*Bangladesh Journal of Physics, Vol. **28**, Issue 2, pp. 59-68, December 2021*

EFFECT OF Cr AS A GRAIN GROWTH INHIBITOR ON CRYSTALLIZATION KINETICS FOR $Fe_{73.5-x}Cr_xCu_1Nb_3Si_{13.5}B_9$ (x = 1, 5, 10, 12.5, 17.5)

M. M. RANA[1], A. Z. ZIAUDDIN AHMED[2], MD. SAROWAR HOSSAIN[3*], M. R. HASSAN[4], M. H. REZVI[5,6], M. N. I. KHAN[7], S. MANJURA HOUQUE[7], M. A. HAKIM[6]

[1]*Department of Physics, Mohammadpur Kendriya College, Dhaka-1207, Bangladesh*
[2]*Department of Basic Sciences, Primeasia University, Dhaka-1213, Bangladesh*
[3]*Department of Physics, Faculty of Science and Technology (FST), American International University-Bangladesh (AIUB), Dhaka-1229, Bangladesh*
[4]*Rooppur Nuclear Power Plant, Pabna 6620, Bangladesh*
[5]*North Carolina State University, Raleigh NC 27695, USA*
[6]*Dept. of NCE, Bangladesh University of Engineering & Technology, Dhaka-1000, Bangladesh*
[7]*Material Science Division, Atomic Energy Centre, Dhaka 1000, Bangladesh*

[*]*Corresponding author e-mail: sakil_phy@aiub.edu*

Received on 30.09.2021, Revised received on 18.11.2021, Accepted for publication on 29.11.2021

DOI: https://doi.org/10.3329/bjphy.v28i2.79345

ABSTRACT

Nanocrystalline Finemet© alloys of composition $Fe_{73.5-x}Cr_xCu_1Nb_3Si_{13.5}B_9$ with x = 1, 5, 10, 12.5, 17.5 were synthesized using the melt spinning technique to study the impact of chromium (Cr) as a grain growth inhibitor on the crystallization kinetics. The alloys were studied under several heat treatments starting from the as-cast to 600°C and the amorphousity of the ribbons is reduced as well as the nucleation of crystallizations starts. Differential Scanning Calorimetry (DSC) analysis shows that increasing Cr content shifts the crystallization temperatures to higher values, enhancing thermal stability. Moreover, the X-ray diffraction (XRD) and Field Emission Scanning Electron Microscopy (FESEM) confirmed the development of an ultra-fine α-Fe(Si) nanocrystalline phase, with the grain size decreasing as Cr content increased. The evolution of microstructure and thermal properties highlight the role of Cr content in delaying crystallization and reducing grain growth, thus improving the nanocrystalline state of the material. These findings provide insights into optimizing Fe-Si-B-based nanocrystalline alloys for advanced applications by balancing thermal treatments and Cr concentration.

Keywords: *Amorphous ribbon, Finemet, Nanocrystalline alloy, Metglass, Annealing*

1. INTRODUCTION

The Finemet® alloy with the composition $Fe_{73.5}Cu_1Nb_3Si_{13.5}B_9$ is identified as a metglass and has demonstrated excellent capabilities in electronic, magnetic, and power electrical engineering applications [1-3]. Finemet® alloys find application in a wide range of core-laminated products such as large power distribution transformers, generators, and motors [4, 5]. Generally, the ribbon-shaped Finemet® alloy is produced by the melt-spinning technique and the as-cast product is structurally amorphous [6-11]. N. Iturriza et al. reported that the melt-spun ribbon of $Ni_5Fe_{68.5}Cu_1Nb_3Si_{13.5}B_9$ composition was 25 μm in thickness and 2 mm in width along with an amorphous structure [12]. However, annealing of this alloy above the recrystallization temperature (>520°C) produces ultra-fine α-Fe(Si) nanocrystallites of DO_3 structure in the amorphous precursor [12, 13]. These nanocrystalline grains embedded in the residual amorphous matrix make up the basic microstructure which allows Finemet® alloys to display incredibly low coercive field values (~1 A/m) [14]. Therefore, the compositional variation and annealing processes of Finemet® alloy have been subjected to intense research over the past 25 years [15-18] in search of promising technological applications based on the correlation between microstructure and soft magnetic properties [19-23]. Crystallization kinetics is widely investigated for these alloys due to enormous phase changes at the time of heat treatment [24-26]. However, the nanocrystals typically range in size from 10 to 20 nm, exhibiting a random orientation of their easy axis and a lower magnetoelastic energy than alloys in an amorphous state. Moreover, the reaction kinetics of Fe-Si-B could be controlled by doping a slight amount of Cu and/or Nb. Here, Cu doping favors the nucleation rate of the BCC α-Fe(Si) phase in the parent structure while Nb

acts as a grain growth inhibitor, and their mutual interaction results in the nanocrystalline structure. Moreover, some other metallic elements (Cr, Ta, Ti, Zr, V, etc.) also act as grain growth inhibitors in the Finmet® alloy [27]. However, the functional properties of the Finemet® alloys need to be controlled over a wide range of temperatures for thermomechanical and thermomagnetic applications [28] like magneto impedance effect-based sensors with very high sensitivity. Previous studies were carried out to meet the desire for high-temperature magnetic properties by the partial substitution of Co for Fe in Finemet® [29-31]. Additionally, it is well known that adding Cr to Fe-Si-B based amorphous alloys improves glass formation, mechanical properties, and thermal stability [26].

Therefore, the article studies the effect of Cr doping in a Finemet® alloy and heat treatment for the synthesized composition $Fe_{73.5-x}Cr_xCu_1Nb_3Si_{13.5}B_9$ with (x = 1, 5, 10, 12,.5, and 17.5). The growth of nanocrystals in these samples due to extensive heat treatments has been severely studied using X-ray diffraction spectra and thermoanalytical techniques. In parallel, the mutation of grain morphologies followed by the crystallization kinematics has been explored.

1. EXPERIMENTAL PROCEDURE

Amorphous ribbons with the nominal composition $Fe_{73.5-x}Cr_xCu_1Nb_3Si_{13.5}B_9$ (x = 1, 5, 10, 12.5, 17.5) were made using the melt spinning technique in a single roller apparatus. At first the alloy ball was created by melting the highly pure raw materials of Fe (99.98%), Cu (99%), Cr (99.5%), and B (99.5%) in an arc furnace after they had been properly weighed. This alloy ball was melted again into a quartz tube crucible surrounded by an induction coil that generates heat around 1,650°C and the whole process was performed in the Ar environment under 10^{-4} mbar pressure. The bottom of the quartz crucible features a rectangular nozzle tip that is 8 mm long and 0.7 mm wide. The nozzle tip's position can be varied relative to the copper wheel surface and a proper ejection of the molten alloy onto the wheel was obtained for the ~0.3 mm perpendicular gap. In addition, the copper wheel was kept rotating at a surface velocity of 30 m/sec, and ejection of melt was performed by applying an overpressure of ~250 mbar Ar supplied from an external reservoir via a nozzle. The resultant ribbon samples were roughly 6 mm in width and 20-22 μm in thickness. Then the crystalline temperatures of as-cast samples were determined by Differential Scanning Calorimetry (DSC) with a heating rate of 20°C per minute. The synthesized ribbons were cut into several pieces, and each piece was annealed for 30 minutes at different temperatures ranging from 480°C to 650°C. The growth of the nanocrystalline phase in the parent sample was studied by the X-ray diffraction (XRD) spectra recorded in a Philips X'Pert Pro with Cu-K α-radiation of $\lambda = 1.54$ Å. Moreover, the grain growth in the synthesized samples was obtained by the Field Emission Scanning Electron microscope (FESEM) of the JEOL JSM 7600F model.

2. RESULT AND DISCUSSIONS

The DSC scan with a continuous heating rate of 20°C/min evaluated the kinetics of crystallization in the as-prepared $Fe_{73.5-x}Cr_xCu_1Nb_3Si_{13.5}B_9$ (x = 1, 5, 10, 12.5, 17.5) ribbons and displayed in Fig. 1. Where, the crystallization of the α-Fe(Si) phase is represented by the first exothermic peak in curves, while the formation of iron boride (Fe-B) is represented by the second peak. In addition, each phase crystallizes over a broad temperature range, and the peak position temperature of DSC thermograph is shifts to the higher side as the Cr content is increased. Therefore, Cr-substituted alloys are more thermally stable. The temperature of the primary exothermic peak temperature and secondary peak temperature are identified as T_{P1} and T_{P2} respectively. The soft magnetic properties correspond to the temperature (T_{x1}) at which primary exothermic heat flow just begins to increase and continues through the maximum peak of α-Fe(Si) nanograin formation. In parallel, the starting temperature of secondary crystallization (T_{x2}) corresponds to the Fe-B phase, which gives the nanocrystalline alloy magnetic hardening. Table 1 represents all of these phase transition temperatures. The larger $\Delta T_x (T_{x2}^{Peak} - T_{x1}^{Peak})$ about 174ºC implies that a single soft magnetic crystalline phase can be precipitated from the amorphous matrix in broad temperature ranges, as is superior to the Finemet® ($\Delta T_x = 115$) °C [32, 33]. The structure of the synthesized composition $Fe_{73.5-x}Cr_xNb_3Cu_1Si_{13.5}B_9$ (x = 1, 5, 10, 12.5, and 17.5) has been revealed by the XRD analysis as illustrated in Fig. 2. In general, the peak at $2\theta \approx 45°$ corresponds to the α-Fe(Si) phase in Finemet® alloy. However, the as-quenched samples of all compositions do not show any remarkable peak in the diffraction pattern except a diffused extended hump observed at $2\theta \approx 45°$ (extended up to 10º) [34, 35].

The diffraction peak becomes sharper and more intense as the annealing temperature (T_a) increases indicating the enlargement of the nanograins [36-38]. It is observed that for x = 1 (Fig. 2(a)) the temperature of nanocrystal formation is quite compatible with the DSC thermogram except the crystallization is initiated at a temperature as low as 500ºC which is lower than T_{p1} (526 ºC). Similarly, the crystallization of the samples with higher Cr content (x = 5, 10, 12.5, and 17.5) starts slowly at a temperature lower than T_{p1} and matures at a higher annealing temperature (T_a). It is clear from these XRD patterns that the onset of the crystallization is hindered as the Cr content rises in the parent composition. Moreover, the crystallization process for the samples with x = 12.5 and 17.5 becomes extremely slow and insignificant until T_a reaches 570°C which ensures the thermal stability for higher Cr content [39] doping.

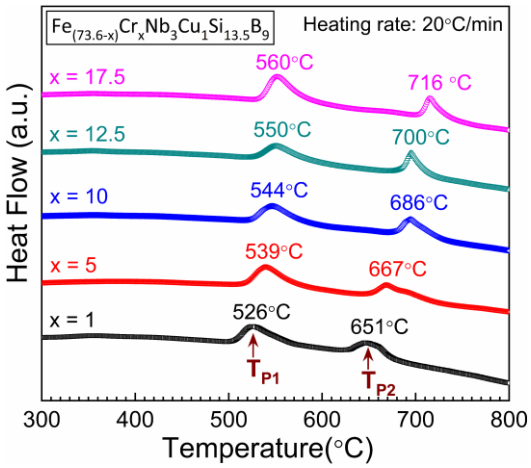

Fig. 1. DSC thermograms of amorphous ribbons $Fe_{73.5-x}Cr_xCu_1Nb_3Si_{13.5}B_9$ alloys where x = 1, 5, 10, 12.5, and 17.5.

Table 1: Phase transition temperatures for $Fe_{73.5-x}Cr_xCu_1Nb_3Si_{13.5}B_9$ (x = 1, 5,10, 12.5 and 17.5) showing crystallization on set temperatures, primary (T_{x1}) and secondary (T_{x2}) peak with peak temperature of primary (T_{p1}) and secondary peak estimated from DSC curve.

Content (x)	T_{x1} (ºC)	T_{p1} (ºC)	T_{x2} (ºC)	T_{p2} (ºC)	$\Delta T_x\left(T_{x2}^{Peak} - T_{x1}^{Peak}\right)$ (ºC)
1	494	526	640	651	146
5	509	539	652	667	143
10	514	544	667	686	153
12.5	517	550	675	700	158
17.5	524	560	698	716	174

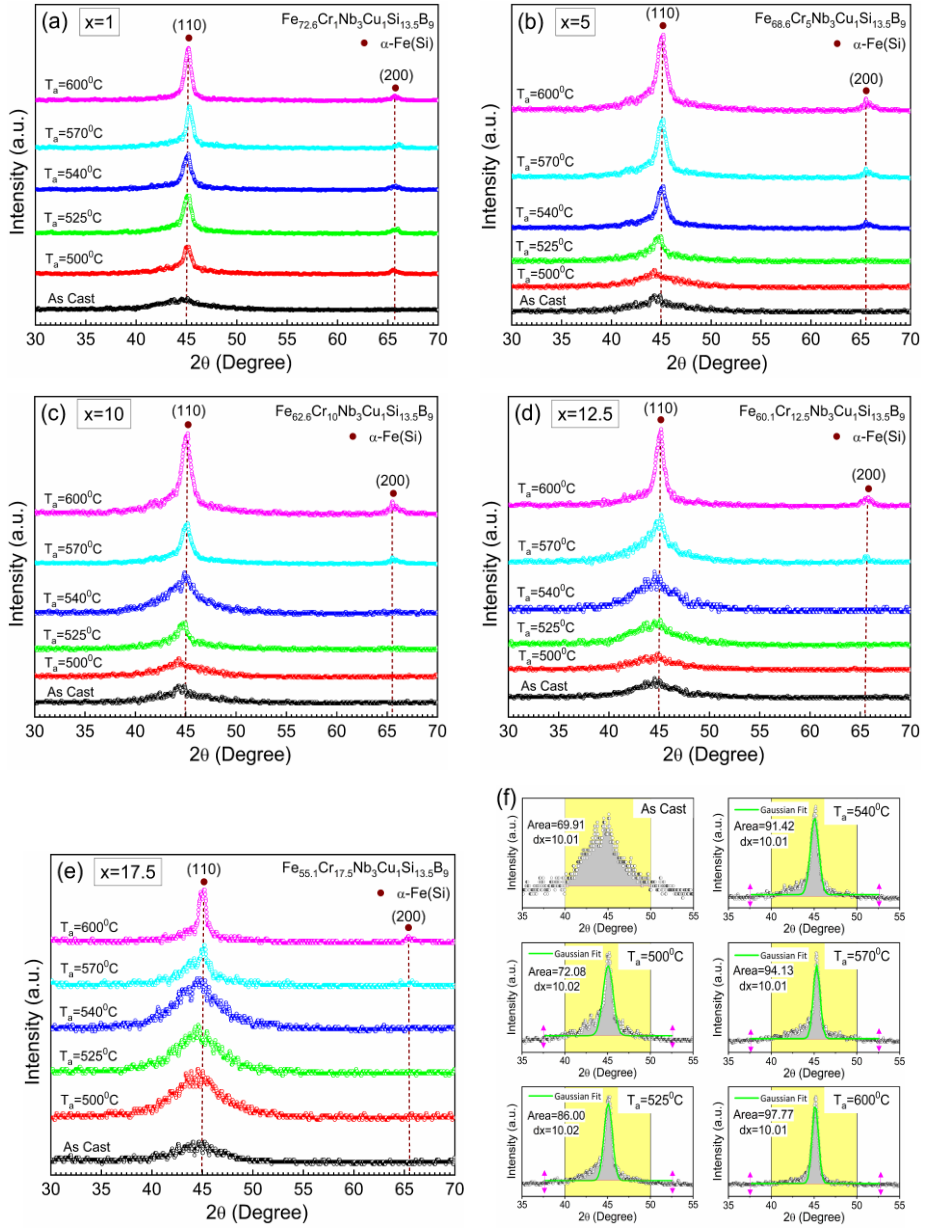

Fig. 2. XRD pattern at different annealing temperatures of $Fe_{73.5-x}Cr_xNb_3Cu_1Si_{13.5}B_9$ alloys for **(a)** x = 1, **(b)** x = 5, **(c)** x = 10, **(d)** x = 12.5 and **(e)** x = 17.5 **(f)** integral intensities of diffraction peaks at different temperature obtained for x = 1 sample.

It could be manifested from the above discussion that the crystalline volume fraction (V_{cry}) is increased due to heat treatment where V_{cry} can be determined from the XRD peaks following the equation [33, 40]

$$V_{cry} = \frac{I_{cry}}{I_{cry} + I_{am}} [1]$$

where, the integrated phase intensities of crystalline and amorphous structure are represented by I_{cry} and I_{am} respectively. Fig. 2(f) represents the integral intensities determined by the mathematical analysis of the area under curve calculation. Apart from these, the full width at half maximum (β) for (110) peak has been obtained by Gaussian fitting as shown in Fig 2(f) and the crystallite size (D) has been calculated from Scherrer's formula $(D = 0.9\,\lambda/\beta cos\theta)$ [41].

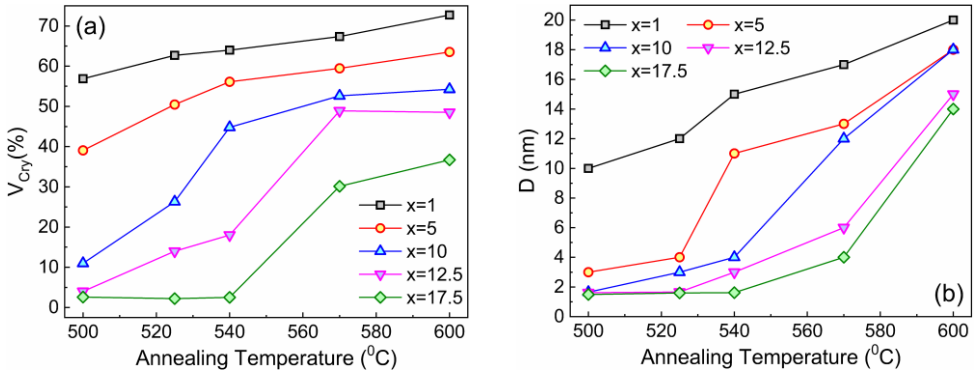

Fig. 3. Annealing effect on structure showing **(a)** variation of crystalline volume fraction (V_{cry}) and **(b)** crystallite size (D) for $Fe_{73.5-x}Cr_xNb_3Cu_1Si_{13.5}B_9$ alloys where, *x*=1, 5, 10, 12.5, and 17.5.

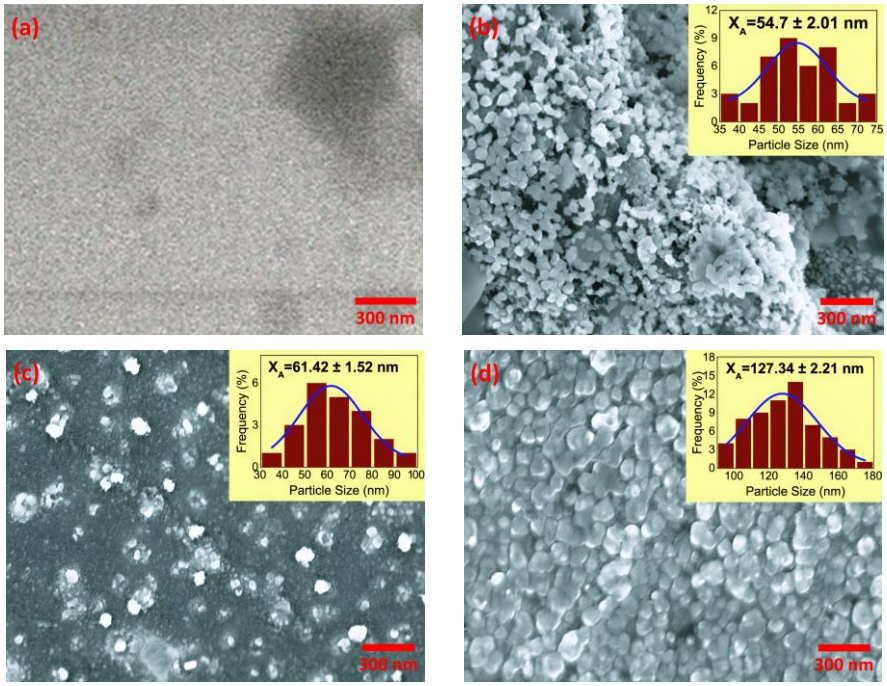

Fig. 4. FESEM microstructure of $Fe_{73.5-x}Cr_xNb_3Cu_1Si_{13.5}B_9$ where *x* = 1 at (a) as cast and annealed at temperatures (b) 480ºC, (c) 520ºC and (d) 550ºC.

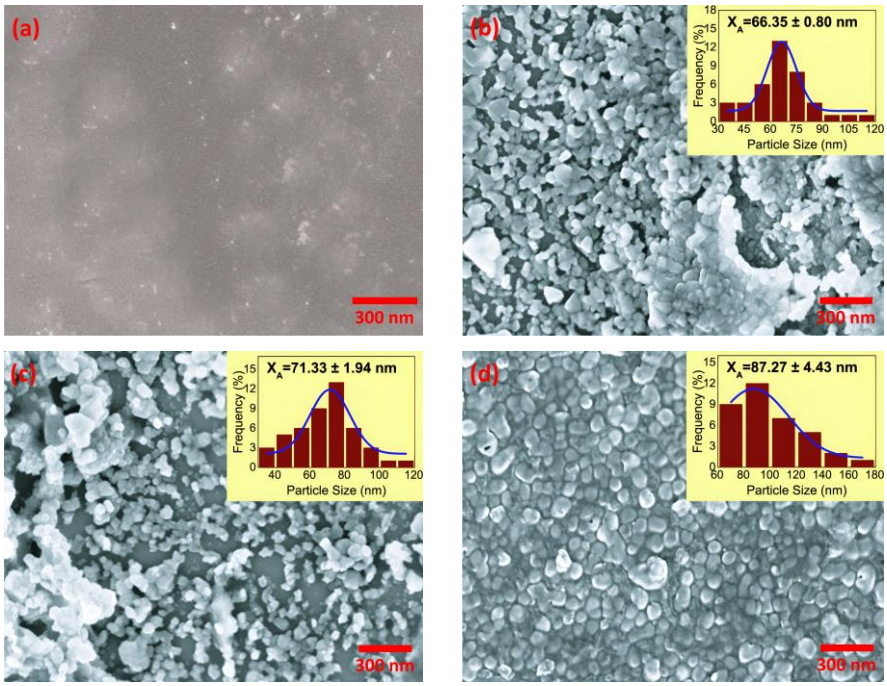

Fig. 5. FESEM microstructure of $Fe_{73.5-x}Cr_xNb_3Cu_1Si_{13.5}B_9$ where x = 5 at **(a)** as cast and annealed at temperatures **(b)** 500°C, **(c)** 540°C and **(d)** 570°C.

The variations of V_{cry} and crystallite size (D) with respect to annealing temperature (T_a) are depicted in the Fig. 3(a) and 3(b) respectively and both are increased with T_a. However, the lower value of D is obtained for the high amount of Cr content attributed to the delayed crystallization due to excess Cr [42]. Furthermore, Fig. 3(a) confirms a high amount V_{cry} for the samples with lower Cr content (x = 1, 5), and a slower increase of V_{cry} for heat treatment is achieved for the samples x=10, 12.5, and 17.5. Therefore, Cr behaves as an active obstacle for the crystallization of Finemet® though annealing helps for the growth of nanocrystals in the alloy. Additionally, the microstructures of the studied samples are also concomitant to nanocrystal growth due to heat treatment. The microstructure of the sample x=1 for $T_a = 0$°C, 480°C, 520°C, and 550°C are displayed in Fig. 4(a-d) where the clear background of the as-cast sample (Fig. 4(a)) exhibits no evidence of crystallization.

The other as-cast sample (x = 5, 10, 12.5, and 17.5) exhibits similar behavior, and grain growth is seen for annealing these samples. Therefore, the size of different grains of the studied samples was determined by the ImageJ 1.50i software using line interpolation and a calibration method. Then the average size of the grains (X_A) has been obtained from the Gaussian fitting of the size distribution as depicted by the inset of microstructures (Fig. 4-6). Table 2 represents the values of X_A for all studied samples and the values are concomitant to the XRD results. For the sample x=1, cluster-like grains are visible in Fig. 4(b) at $T_a = 480$°C which is identified as the stage leading to the start of crystallization along with agglomeration. Furthermore, Fig. 4(c) illustrates the microstructure of the sample annealed at 520°C where nanograins are well developed. However, grains are separated from each other indicating less agglomeration.

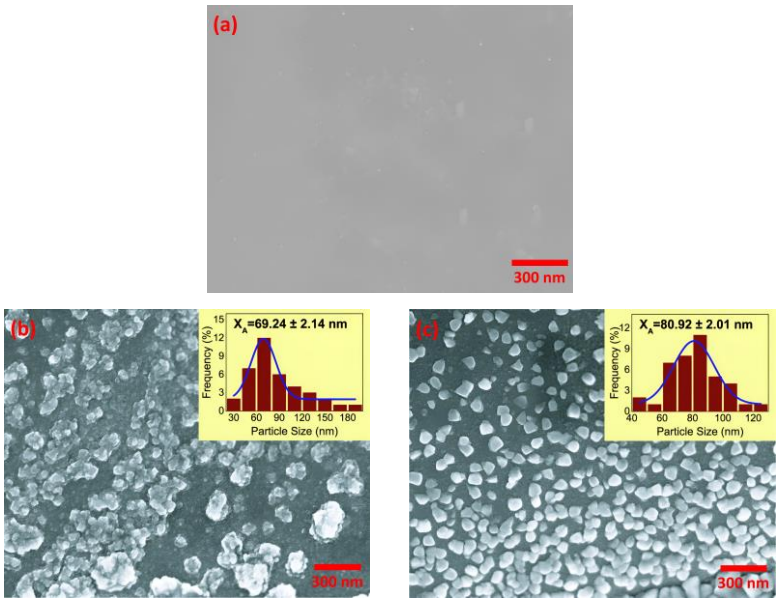

Fig. 6. FESEM microstructure of $Fe_{73.5-x}Cr_xNb_3Cu_1Si_{13.5}B_9$ where x = 10 **(a)** as cast and annealed at temperatures **(b)** 540ºC, and **(c)** 570ºC.

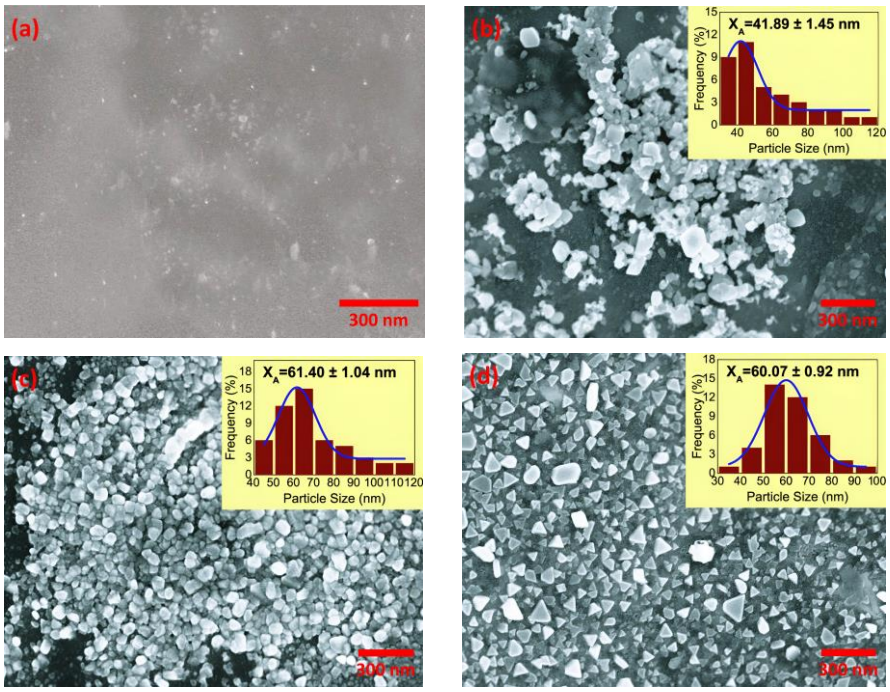

Fig. 7. FESEM microstructure of $Fe_{73.5-x}Cr_xNb_3Cu_1Si_{13.5}B_9$ where x = 12.5 **(a)** as cast and annealed at temperatures **(b)** 540ºC, **(c)** 570ºC and **(d)** 600ºC.

Finally, the sample x = 1 annealed at 550ºC represents a complete crystallization with the larger grains which brings the grains closer. The microstructures of the sample with x=5 in as cast and annealed at $T_a = 500$, 540, and 570°C are displayed in Fig. 5(a-d) where the crystallization has begun at 500°C. For the sample x=10 the microstructures in Fig. 6 represent the grain growth in this sample and the grains are well-matured for $T_a = 570$°C having average grain sizes~81 nm.

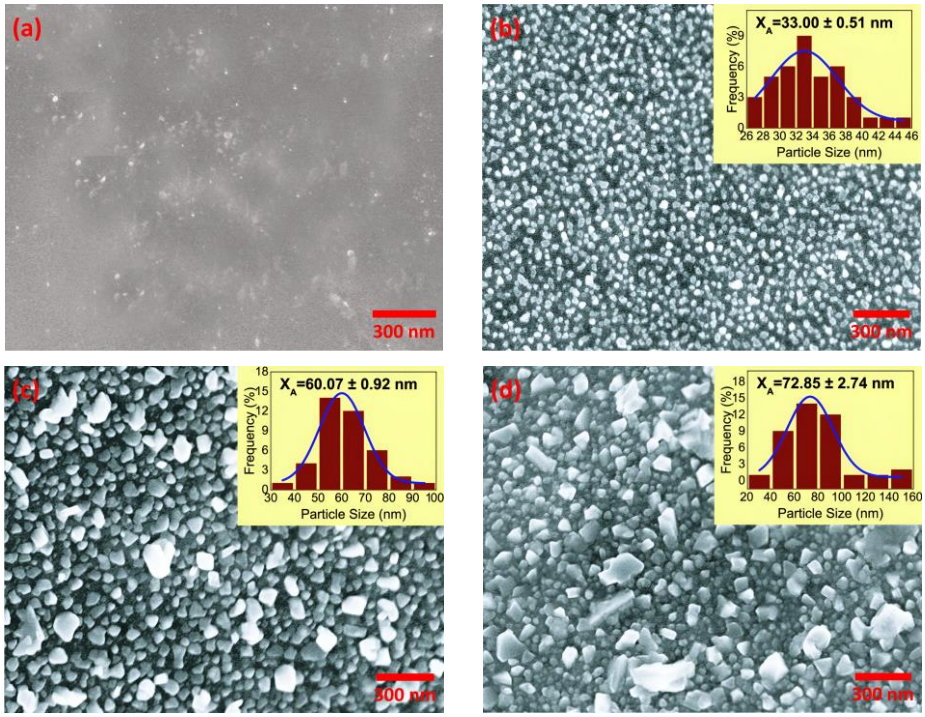

Fig. 8. FESEM microstructure of $Fe_{73.5-x}Cr_xNb_3Cu_1Si_{13.5}B_9$ where x = 17.5 **(a)** as cast and annealed at temperatures **(b)** 570ºC, **(c)** 600ºCand **(d)** 650ºC.

Table 2: Average grain size (X_A) estimated from SEM image of $Fe_{73.5-x}Cr_xCu_1Nb_3Si_{13.5}B_9$ with the variation of Cr content and annealing temperature, T_a.

x =1		x = 5		x = 10		x = 12.5		x = 17.5	
T_a (ºC)	X_A (nm)	T_a (ºC)	X_A (nm)	X_A (ºC)	X_A (nm)	X_A (ºC)	X_A (nm)	T_a (ºC)	X_A (nm)
480	54.7	500	66.35	550	69.24	540	41.89	570	33
520	61.42	550	71.33	570	80.92	570	61.40	600	55.44
550	127.34	570	87.27	--	--	600	60.07	650	72.85

According to DSC data, it is found that the crystallization of the peak temperature for the sample of concentration x = 10 is $T_{P1} =$ 54 °C and its crystallization onset temperature is found to be $T_{x1} =$ 51 °C. Additionally, the microstructure development of the sample with Cr = 12.5 after annealing at 540°C, 570°C, and 600°C as displayed in Fig. 7(b-d), and the matured grains are demonstrated for $T_a = 600$ºC with ~ 60nm size. Finally, the microstructure of the sample with Cr = 17.5 in Fig. 8(b) represents the unique nanograins with ~33 nm annealed at 570ºC while grains are enlarged to ~73nm for annealed at 650°C (Fig. 8(d)). It is evident for the microstructure of $Fe_{73.5-x}Cr_xNb_3Cu_1Si_{13.5}B_9$ (x = 1, 5, 10, 12.5, and 17.5) that these samples are highly influenced by the

concentration of Cr and the thermal treatment temperature. The crystallization event is more difficult to occur at higher Cr contents, indicating that Cr has a thermal stability effect that prevents crystallization [43].

3. CONCLUSIONS

The interaction between annealing temperature and grain growth inhibitors such as Cr can optimize the nanocrystalline state in Finemet alloys. As Cr content increases in a Finemet alloy, the crystallization temperature shifts across a broad range. At higher Cr levels, the crystallization rate slows down and clusters together. The crystalline volume fraction reaches a saturation point as the annealing temperature rises with higher Cr levels. The shift in the crystallization temperature peak with increasing Cr content indicates that Cr-substituted alloys have improved thermal stability.

REFERENCES

[1] T. H. Kim, K. K. Jee, Yoon B. Kim, D. J. Byun, J. H. Han, J. Magn. And Magn. Mater. **322** (2010) 2423.
[2] K. H. Maria, S. Islam, S. Choudhury, M. A. Hakim, D. K. Saha, S. M. Hoque, Int. Nano Lett. **1** (2011) 97.
[3] S. P. Mondal, M. M. Rahman, S. S. Sikder and M. A. Hakim, J. Engin. Sci. **02** (2010) 59.
[4] S.V. Ponnaluri, R. Cherukuri, P.A. Molian, J. Mater. Process. Technol. **112** (2001) 199-204.
[5] J. Qin, P. Yang, W. Mao, F. Ye, J. Magn. Magn. Mater. **393** (2015) 537-543.
[6] A. A. Shirzadi, T. Kozieł, G. Cios, P. Bała, **264** (2019) 377-381.
[7] X. D. Liu, X.B. Liu, Z. Appl. Phys. A. **82** (2006) 339-343.
[8] D. Jiang, B. Zhou, B. Jiang, B. Ya, X. Zhang, Phys. Status Solidi A **214** (2017) 1700074.
[9] L. -j. Li, Z. Wang, Y. Han, Mater. Lett. **185** (2016) 235-238.
[10] D.-h. Wen, L.-z. Yin, Z.-y. Piao, C.-d. Lu, G. Li, Q.-h. Leng, Int. J. Heat Mass Transf. **121** (2018) 775–787.
[11] W. Dong-Hui, Y. Lin-Zhi, P. Zhong-Yu, L. Cong-Da, L. Gang, L. Qiao-Hui, Int. J. Energy Res. **41** (2017) 2184-2193.
[12] N. Iturriza, C. García, L. Fernández, J. J. del Val, J. González, J. M. Blanco, G. Vara, and A. R. Pierna, J. Appl. Phys. **99** (2006) 08F104.
[12] M. E. McHenry, M. A. Willard, D. E. Laughlin, Prog. Mater. Sci. **44** (1999) 291-433.
[13] G. Herzer, J. Magn. Magn. Mater **112** (1992) 258.
[14] J. González, O. A. Chubykalo and J. M. González, in Encyclopedia of Nanoscience and Nanotechnology edited by H. S. Nalwa (American Scientific, Baltimore), **10** (2004) 1.
[15] T. Gheiratmand, H. R. Madaah Hosseini, J. Magn. Magn. Mater. **408** (2016) 177-192
[16] H. R. Lashgari, D. Chu, Shishu Xie, Huande Sun, M. Ferry, S. Li, J. Non-Cryst. 391 (2014) 61-82.
[17] J. Wang, Z. Wang, Y-Y Jia, R-M Shi, J. Magn. Magn. Mater. 328, (2013) 62-65.
[18] M. Ohnuma, D.H. Ping, T. Abe, H. Onodera, K. Hono, J. Appl. Phys 105 (2009) 9186-9194.
[19] H. Fukunaga, T. Yanai, H. Tanaka, M. Nakano, K. Takahashi, and Y. Yoshizawa, J. Appl. Phys. **87** (2000) 7103
[20] J. S. Blázquez, V. Franco, C.F. Conde, A. Conde, J. Ferenc, T. Kulik, L.F. Kiss, J. Appl. Phys. **105** (2009) 093928.
[21] K. Rajat, S. S. Roy, S. J. Kernion, M. E. McHenry, J. Appl. Phys. **111** (2012) 07301.
[22] M. Müller, H. Grahl, Mattern N.U. Kühn, B. Schnell, J. Magn. Magn. Mater. 160 (1996) 284-286.
[23] Z. Wang, J. Yang, Y-M Han, D-X. Zhang, B. Fu, R-C Ye, J. Appl. Phys. **107** (2010) 09A308.
[24] N. Bayri, T. Izgi, H. Gencer, P. Sovak, M. Gunes, and S. Atalay, J. Non-Cryst. **355** (2009) 12.
[25] Z. Wang, K. Y. He, J. Jin, J. He, L. Zhang, H. -W. Zhang, and B.-G. Shen, Mater. Sci. Eng.: A **304-306** (2001) 1046.
[26] Q. Z. Zhi, B. S. Dong, W. Z. Chen, and K. Y. He, Mater. Sci. Eng.: A **448** (2007) 249.
[27] Bernhard Wittmann, Wolf-Dieter Schubert, Benno Lux, Int. J. Refract. Met. Hard Mater. **20(1)** (2002) 51-60.
[28] V. A. Lukshina, ; N. V. Dmitrieva, E. G. Volkova, D.A. Shishkin, Phys. Met. Metallogr. **120** (2019) 320-324.
[29] Y. M. Han, Z. Wang, X. H. Che, X. -G. Chen, W. -R. Li, and Y.-L. Li, Mater. Sci. Eng., B **156** (2009) 57.
[30] J. S. Blázquez, V. Franco, C. F. Conde, A. Conde, J. Ferenc, T. Kulik, and L. F. Kiss, J. Appl. Phys. **105** (2009) 093928.

[31] C. Gómez-Polo, J. I. Pérez-Landazabal, V. Recarte, J. Campo, P. Marín, M. López, and A. Hernando, Phys. Rev. B **66** (2002) 012401.
[32] T. H. Noh, M. B. Lee, H. J. Kim, and I. K. Kang, J. Appl. Phys. 67 (1990) 5568.
[33] Z. Wang, J. Yang, Y. Han, D. Zhang, B. Fu, and R-C Ye, J. Appl. Phys. **107** (2010) 09A308.
[34] E. Hossain, S. Choudhury, M. A. Bhuiyan, K. H. Maria, M. H. Mesbah Ahmed, D. K. Saha, and M. A. Hakim, Advanced Science Focus **2** (2014) 12.
[35] P. Sharma, and A. Gupta, Section B: Beam Interactions with Materials and Atoms, **244** (2006) 105.
[36] X. B. Liang, T. Kulik, J. Ferenc, M. Kowalczyk, G. Vlasák, W. S. Sun, and B. S. Xu, Physica B **370** (2005) 151.
[37] C. Zhang, Z. Zhu, and H. Zhang, J. Phys. Chem. Solids, **110** (2017) 152.
[38] S. Islam, K. H. Maria, S. Choudhury, M. A. Hakim, D. K. Saha, Turk. J. Phys. **36** (2012) 253.
[39] Millán, M., C. F. Conde, and A. Conde, J Mater Sci. **30** (1995) 3591.
[40] X. Y. Zhang, F. X. Zhang, J. W. Zhang, W. Yu, M. Zhang, J. H. Zhao, R. P. Liu, Y. F. Xu, and W. K. Wang, J. Appl. Phys. **84** (1998) 1918.
[41] Jörg F. Löffler, Intermetall. **11** (2003) 529.
[42] M. S. Mahmud, Asian Transac.Sci. Technol. **01** (2013) 03.
[43] J-J. Han, C-P. Wang, S-Z. Kou, and X-J. Liu, Transac. Nonferrous Met. Soci. China **23** (2013) 148.